

This is a repository copy of *Kinetic ballooning modes as a constraint on plasma triangularity in commercial spherical tokamaks*.

White Rose Research Online URL for this paper:

<https://eprints.whiterose.ac.uk/189491/>

Version: Published Version

Article:

Davies, R., Dickinson, D. orcid.org/0000-0002-0868-211X and Wilson, H. orcid.org/0000-0003-3333-7470 (2022) Kinetic ballooning modes as a constraint on plasma triangularity in commercial spherical tokamaks. *Plasma Physics and Controlled Fusion*. 105001. ISSN 1361-6587

<https://doi.org/10.1088/1361-6587/ac8615>

Reuse

This article is distributed under the terms of the Creative Commons Attribution (CC BY) licence. This licence allows you to distribute, remix, tweak, and build upon the work, even commercially, as long as you credit the authors for the original work. More information and the full terms of the licence here:

<https://creativecommons.org/licenses/>

Takedown

If you consider content in White Rose Research Online to be in breach of UK law, please notify us by emailing eprints@whiterose.ac.uk including the URL of the record and the reason for the withdrawal request.

PAPER • OPEN ACCESS

Kinetic ballooning modes as a constraint on plasma triangularity in commercial spherical tokamaks

To cite this article: R Davies *et al* 2022 *Plasma Phys. Control. Fusion* **64** 105001

View the [article online](#) for updates and enhancements.

You may also like

- [Pedestal properties of H-modes with negative triangularity using the EPED-CH model](#)
A Merle, O Sauter and S Yu Medvedev
- [To dee or not to dee: costs and benefits of altering the triangularity of a steady-state DEMO-like reactor](#)
J.A. Schwartz, A.O. Nelson and E. Kolemen
- [Intermediate \$n\$ mode stability in the negative triangularity tokamaks](#)
Linjin Zheng, M.T. Kotschenreuther and F.L. Waelbroeck



IOP | ebooks™

Bringing together innovative digital publishing with leading authors from the global scientific community.

Start exploring the collection—download the first chapter of every title for free.

Kinetic ballooning modes as a constraint on plasma triangularity in commercial spherical tokamaks

R Davies* , D Dickinson  and H Wilson 

York Plasma Institute, University of York, Heslington, YO10 5DD York, United Kingdom

E-mail: bob.davies@york.ac.uk

Received 26 April 2022, revised 6 July 2022

Accepted for publication 1 August 2022

Published 19 August 2022



CrossMark

Abstract

To be economically competitive, spherical tokamak (ST) power plant designs require a high β (plasma pressure/magnetic pressure) and sufficiently low turbulent transport to enable steady-state operation. A novel approach to tokamak optimisation is for the plasma to have negative triangularity, with experimental results indicating this reduces transport. However, negative triangularity is known to close access to the ‘second stability’ region for ballooning modes, and thus impose a hard β limit. Second stability access is particularly important in ST power plant design, and this raises the question as to whether negative triangularity is feasible. A linear gyrokinetic study of three hypothetical high β ST equilibria is performed, with similar size and fusion power in the range 500–800 MW. By closing the second stability window, the negative triangularity case becomes strongly unstable to long-wavelength kinetic ballooning modes (KBMs) across the plasma, likely driving unacceptably high transport. By contrast, positive triangularity can completely avoid the ideal ballooning unstable region whilst having reactor-relevant β , provided the on-axis safety factor is sufficiently high. Nevertheless, the dominant instability at long wavelength still appears to be the KBM, though it could be stabilised by flow shear.

Keywords: spherical tokamak, kinetic ballooning mode, plasma microinstability, positive triangularity, negative triangularity

(Some figures may appear in colour only in the online journal)

1. Introduction

Commercial viability of fusion reactors require low capital cost and high plasma performance. In these regards, a particularly promising class of design is the spherical tokamak (ST),

which differs from a conventional tokamak by having a smaller aspect ratio ($A \equiv R_0/r_{\text{minor}} < \sim 2$, where R_0 is the major radius and r_{minor} the minor radius). This reduces the (radial) machine size (hence cost), increases the plasma β (plasma pressure/magnetic pressure) [1] and has been found to improve some plasma stability properties [2, 3]. A recent study predicted an increase in fusion triple product $nT\tau_E$ (where n , T and τ_E are the density, temperature and energy confinement time respectively) by a factor of 3 could be achieved in an ST compared to a conventional tokamak with similar values of fusion power and field strength but different machine size [4]. STs are thus receiving significant attention in the fusion community. Several devices have recently been built

* Author to whom any correspondence should be addressed.



Original Content from this work may be used under the terms of the [Creative Commons Attribution 4.0 licence](https://creativecommons.org/licenses/by/4.0/). Any further distribution of this work must maintain attribution to the author(s) and the title of the work, journal citation and DOI.

or upgraded, such as NSTX-U [5], ST40 [6] and MAST-U [7]. Others are currently being designed or built, such as SMART [8] and STEP [9]. However, reactor-relevant equilibria must have sufficiently low turbulent transport to provide sufficient confinement time to maintain density and temperature profiles with modest heating power. The tuning of ST equilibria to optimise turbulence is an area of active research.

A novel approach to optimisation is ‘negative triangularity’, whereby the plasma poloidal cross section resembles a backward ‘D’ (rounded on the inboard, high-field side). Experiments in TCV [10] and DIII-D [11] reported reduced turbulence with negative triangularity plasmas. For DIII-D, which operated negative triangularity in a limiter configuration, stored energy increased by 25% and electron energy confinement time by 26% compared to L-mode positive triangularity shots. However, no L-H transition occurred for the negative triangularity discharge, even at high heating power. This was found to coincide with the (modelled) H-mode pedestal being unstable to (toroidal mode number) $n = \infty$ ideal ballooning modes (IBMs) [12], an instability driven by normalised plasma pressure gradient $\partial\beta/\partial\psi$ (where ψ is the poloidal flux function). Saarelma *et al* [12] proposed that L-H transition in negative triangularity is only achievable when the pedestal is stable to IBMs for all pressure gradients; the so-called ‘second stability window’. Without second stability access, strongly driven turbulence above a critical $\partial\beta/\partial\psi$ prevents pedestal formation and H-mode is suppressed. IBMs are known to be destabilised by negative triangularity [13], and this raises the question of whether negative triangularity is viable in commercial STs, which typically access second stability across the full radius [14].

Although the above discussion portrays IBMs as the responsible instability, the mechanism for the suppression is spatially small (\sim ion Larmor radius) turbulence, for which kinetic effects cannot, in general, be ignored. The relevant instability is therefore the kinetic ballooning mode (KBM) [15, 16], which may be considered the ‘kinetic analogue’ of the IBM. While KBM stability is often assumed to track the IBM, it may be altered by effects such as diamagnetic stabilisation [17] or destabilisation by trapped particles [18]. A kinetic theory is thus required for turbulence studies.

In this paper, we seek to answer whether KBMs prohibit strongly negative triangularity in commercial ST reactors, and whether KBMs are likely to be problematic in positive triangularity ST equilibria. To do this, we use gyrokinetic simulations to examine the ion-scale instabilities in three strongly shaped hypothetical ST equilibria, constructed with a commercial reactor in mind.

2. Equilibria selected

Our equilibria (which are publicly available [19]) were generated by the fixed-boundary equilibrium code SCENE [20], which simultaneously solves the Grad–Shafranov equation and the neoclassical current contributions to generate an equilibrium with self-consistent current profiles. Some important

Table 1. Some key quantities for the equilibria used in this study.

	‘–ve tri’	‘high $q0$ ’	‘low $q0$ ’
Aspect ratio	1.67	1.67	1.67
R_0	2.50	2.50	2.50
$q0$	2.58	2.71	1.38
q_{LCFS}	4.50	8.97	9.16
δ_{LCFS}	–0.300	0.543	0.543
κ_{LCFS}	2.80	2.80	2.80
β	18.1%	18.6%	18.5%
β_N	4.21	5.47	5.50
Toroidal current (MA)	16.5	16.5	16.5
Toroidal B (magnetic axis) (T)	1.93	1.83	1.83
Plasma volume (m ³)	310	287	288
Heating power (MW)	60	60	60
Fusion power (MW)	514	808	839

quantities regarding these equilibria are shown in table 1, and radial profiles of electron density n_e , electron temperature T_e and safety factor q in figure 1. For simplicity we take $T_e = T_i$. Since fusion α s preferentially heat electrons, it is plausible that T_e would exceed T_i in practice. However, the focus of our study is ballooning modes, which are typically sensitive to the total pressure gradient rather than to the contribution of individual species.

The equilibria were constructed with identical major radius and elongation on the last closed flux surface (LCFS), total toroidal current and auxiliary heating/current drive power. The density and temperature profiles are reasonable models, but not the results of transport simulations. These equilibria operate in H-mode, though the conclusions regarding core microstability should be broadly applicable to commercially relevant L-mode plasmas. Another benefit of using H-mode equilibria is that it may give indication as to whether L-H transition is feasible (similar to Saarelma *et al* [12]), although that is not the focus of this work.

Two equilibria (which we label ‘high $q0$ ’ and ‘low $q0$ ’) were given strongly positive LCFS triangularity (0.543), the main difference being their on-axis safety factor $q0$. Both are unstable to external kink modes, though the ‘high $q0$ ’ case is stabilised by a wall at $r_{wall} = 1.4r_{minor,LCFS}$. The ‘low $q0$ ’ case remains unstable to $n = 1$ external kink even at $r_{wall} = r_{minor,LCFS}$, and so is not a robust equilibrium from a magneto-hydrodynamic (MHD) perspective. The third (‘–ve tri’) has LCFS triangularity of –0.3. Although this leads to a greater plasma volume, the density pedestal gradient is lower, resulting in a reduced fusion power of 40% compared to the positive triangularity cases. MHD stability has not been examined for this equilibrium.

3. Simulation tools

For this work, we use the freely available local gyrokinetic software GS2 [21] to (a) calculate the ideal ballooning stability for our equilibria and (b) perform local δf gyrokinetic simulations. These are described in the following sections.

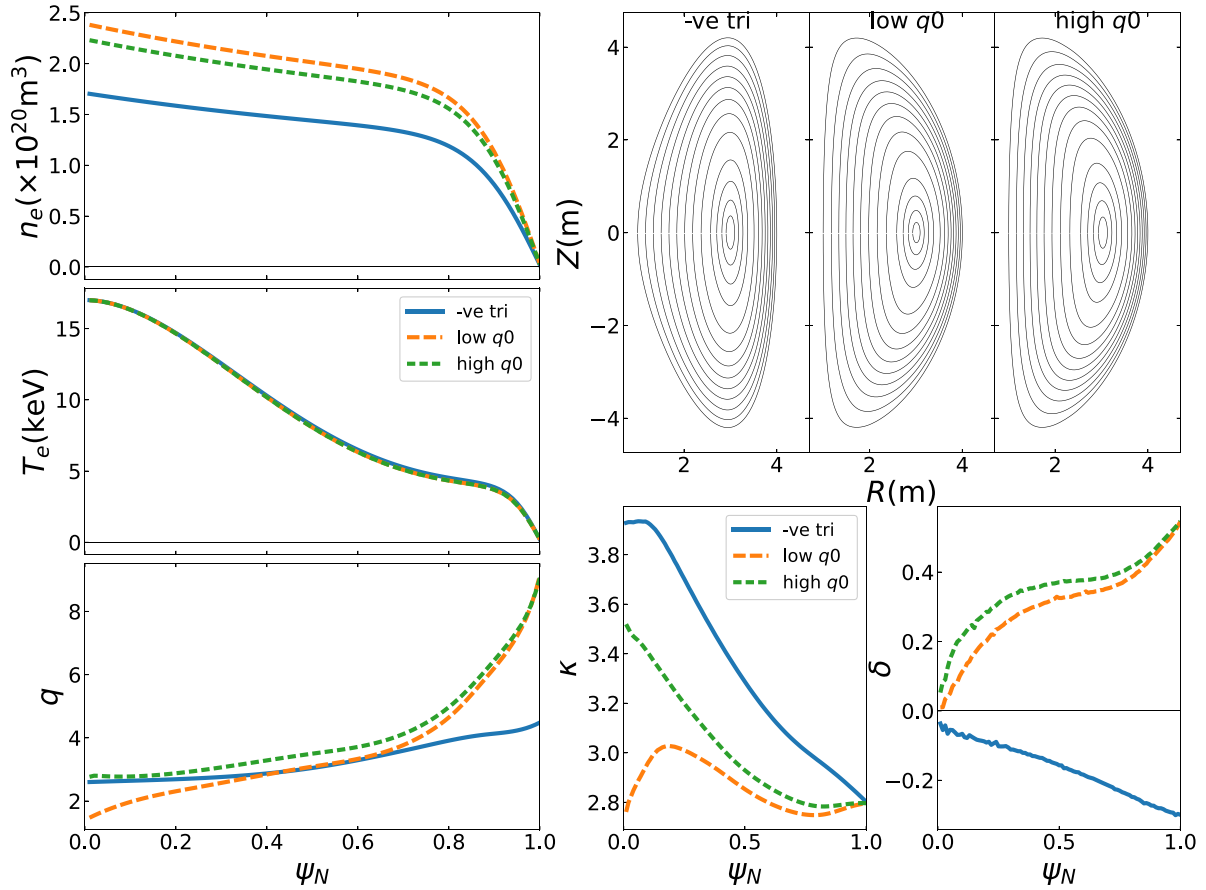


Figure 1. Left column: kinetic profiles n_e and T_e and q profile for the three equilibria studied in this work. Right, upper: sample flux surfaces spanning the range $\psi_N = [0.005, 1]$. Right, lower: geometric values of elongation κ and triangularity δ across the radius of each equilibrium.

3.1. Ideal ballooning stability analysis

We calculate the $n = \infty$ ballooning stability using the GS2 module `ideal_ball`, which has previously been used for IBM studies in other devices [22].

An example of IBM stability for a flux surface as a function of normalised magnetic shear $\hat{s} \equiv \partial q / \partial \psi_N$ and normalised pressure gradient $\alpha \equiv \beta \cdot (1/p) \cdot \partial p / \partial \psi_N$ ($\psi_N \equiv \psi / \psi_{\text{LCFS}}$ will be used as our radial coordinate in this work) is shown in figure 2, where we consider the cyclone base case [23]. For $\hat{s} > \hat{s}_{\text{min}}$, the plasma is ballooning unstable for ($\alpha_{\text{crit}}(\hat{s}) < \alpha < \alpha_{2\text{nd}}(\hat{s})$); α_{crit} is the boundary separating the first stable region from the unstable region, and $\alpha_{2\text{nd}}$ separates the unstable and second stable regions. $\hat{s} < \hat{s}_{\text{min}}$ represents the second stability window, in which the flux surface is stable for all α . The window size (i.e. the value of \hat{s}_{min}) is particularly important for ST equilibria (e.g. [14]), since a high core β requires $\alpha(\psi_N)$ to be large, and typically $\alpha > \alpha_{\text{crit}}$ is required.

3.2. Gyrokinetic analysis

We examine the KBM and other microinstabilities using GS2, which numerically advances the linear electromagnetic gyrokinetic-Maxwell equations in the local limit, with A_{\parallel} and B_{\parallel} fluctuations included, and a Fourier transform being applied in the two dimensions perpendicular to the equilibrium

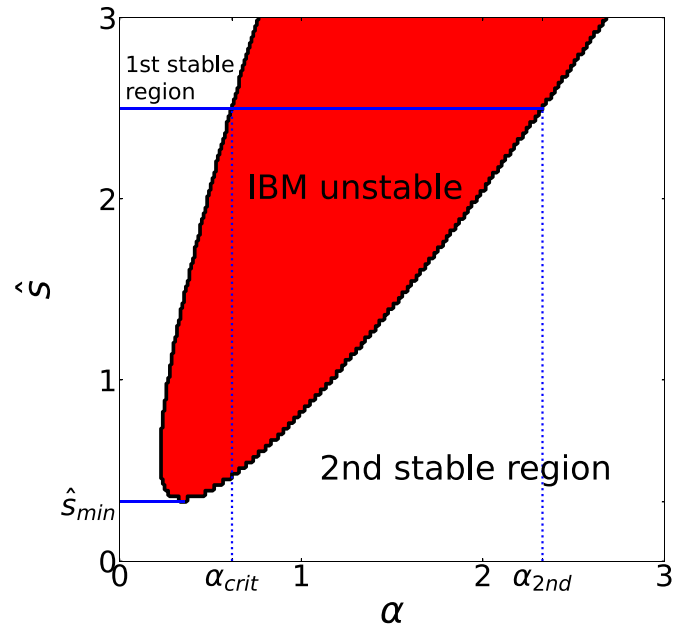


Figure 2. IBM stability as a function of normalised pressure gradient α and magnetic shear \hat{s} for the cyclone base case (CBC).

magnetic field (x and y in GS2 notation; the radial and binormal directions respectively). The equations [24] and the algorithms used to advance them [25] are discussed extensively elsewhere

so are not covered here. In this work we will find the complex frequency $\Omega = \omega + i\gamma$ (where ω is the real frequency and γ the growth rate) of the dominant mode as a function of $(\psi_N, k_y \rho_r, k_x \rho_r)$. k_y is the binormal wavenumber and k_x the radial wavenumber evaluated at the outboard midplane; both are normalised to a ‘reference’ gyroradius, for which we use the proton thermal gyroradius of the surface, $\rho_r(\psi_N) \equiv \sqrt{2T/m_p}/\Omega_p$ where m_p is the proton mass and $\Omega_p \equiv eB_r/m_p$ the proton gyrofrequency, with B_r the reference magnetic field (the toroidal field at the location of the magnetic axis). We will find it helpful to substitute $k_x \rho_r$ with $\theta_0 \equiv k_x/(k_y \hat{s})$ since Ω is periodic in θ_0 . We will also connect $k_y \rho_r$ to toroidal mode number $n = A(\psi_N)(k_y \rho_r)$ where A is a weakly varying function of ψ_N .

The gyrokinetic-Maxwell equations used here assume negligible plasma rotation. In reality, sheared rotation in tokamak plasmas does exist and can stabilise microinstabilities [26]. To gauge the magnitude of this effect, we estimate the Hahn–Burrell shearing rate $|\omega_{HB}|$ [26] by calculating the $\mathbf{E} \times \mathbf{B}$ flow arising from the diamagnetic flow in the equilibrium. That is, we estimate the $\mathbf{E} \times \mathbf{B}$ flow shear from the balance of electric field and pressure gradient forces in the equilibrium, in the absence of externally driven rotation (as expected for reactor-grade tokamak plasmas). The method for this (similar to that used by [27]) is described in appendix A. We have not considered other sources or sinks of plasma flows, such as intrinsic rotation [28, 29] as we lack a simple model applicable to STs. This may moderate the microstability picture.

The results presented here simulate a kinetic electron species and a single ion species with a mass of 2.5 times the proton mass; this effectively simulates a deuterium-tritium (DT) plasma with equal densities of isotopes. Collisions are ignored in this work.

Some discussion is given to numerical parameters, impurities and collisions in appendix B. To summarise, we find that these simulations present a realistic picture for $k_y \rho_r < \sim 1$ over most of the plasma ($\psi_N < \sim 0.9$). Near the edge ($\psi_N > 0.9$), collisionality becomes more important and the strong shaping presents challenges to the calculation of GS2’s θ grid; these edge results should therefore be interpreted qualitatively, rather than quantitatively. Suprathermal α particles were included in the equilibrium calculations, but in the gyrokinetic simulation they were incorporated into the ion species by increasing n_i and ensuring the kinetic profiles matched the prescribed pressure gradient while maintaining $n_i = n_e$ and $T_i = T_e$. The kinetic role of suprathermal α particles would be an interesting area of future research.

4. Stability properties of the negative triangularity equilibrium

In the ‘–ve tri’ equilibrium, we find that the second stability is blocked for the entire plasma ($\hat{s}_{min} < 0$) and $\alpha(\psi) > \alpha_{crit}(\psi)$ (figure 3). As a result, the equilibrium is ideal MHD ballooning unstable over the core. In the pedestal, α strays into the second stable region ($\alpha > \alpha_{2nd}$), coinciding with a sharp drop in the

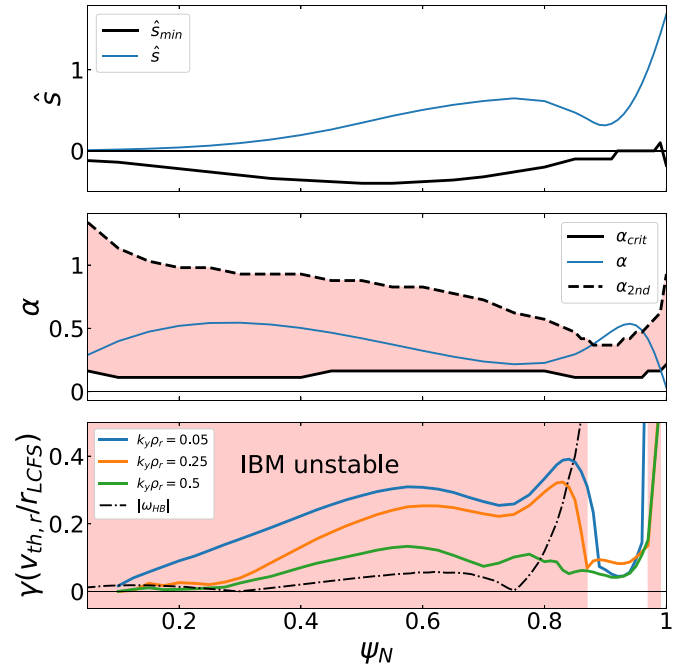


Figure 3. ‘–ve tri’ equilibrium stability properties vs ψ_N . Upper: equilibrium shear (\hat{s}) and second stability ‘window size’ (\hat{s}_{min}). Middle: equilibrium pressure gradient (α , α_{crit} , α_{2nd}); shaded region indicates IBM-unstable plasma parameters. Lower: gyrokinetic growth rate ($\gamma(\psi_N)$) for several $k_y \rho_r$ and $\theta_0 = 0$ (solid lines). Dashed line indicates estimated Hahn–Burrell shearing rate $|\omega_{HB}|$.

normalised gyrokinetic growth rate $\gamma(\psi_N)$ (lower plot). This supports the picture (validated in section 6.1) that, where the plasma is IBM-unstable, long-wavelength KBMs are the dominant instability. It should be noted that the gyrokinetic growth rate γ is normalised to the thermal velocity associated with the flux surface, so the absolute growth rates have a different (but qualitatively similar) trend.

At $\psi_N > \sim 0.97$, there are strongly growing instabilities, as the equilibrium again becomes ballooning-unstable. However, our estimated $|\omega_{HB}|$ is high in this region, so flow shear (as well as collisions) would likely need to be included in simulations to give a realistic picture of stability.

Figure 4 shows $\gamma(k_y \rho_r, \theta_0)$ for several values of ψ_N . For $\psi_N = 0.5, 0.8$, the instability spans a wide range of low $k_y \rho_r$, suggestive of an ‘ideal’ KBM, largely governed by ideal MHD physics [17, 18]. These KBMs are also wide in θ_0 , and thus less easily stabilised by flow shear. $\psi_N = 0.9$ shows the KBM being less unstable for modes with $k_y \rho_r < \sim 0.1$, before the onset of a tearing parity mode at $k_y \rho_r < \sim 0.01$.

Although nonlinear gyrokinetic simulations would be needed to calculate the turbulent fluxes of particles and energy, our linear results indicate that those fluxes would be large. It should be noted that reliable nonlinear results may be difficult to obtain, since electromagnetic nonlinear simulations commonly fail to saturate for equilibria beyond marginal stability [30].

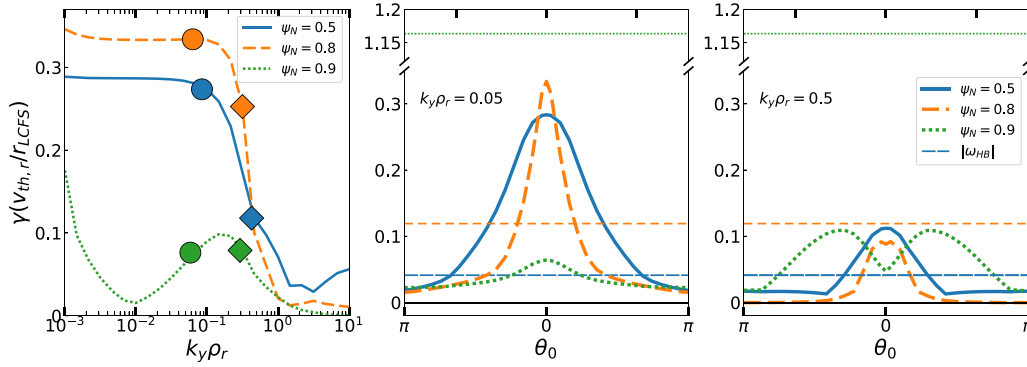


Figure 4. Gyrokinetic growth rate γ for several flux surfaces for ‘-ve tri’ equilibrium. Left: $\gamma(k_y \rho_r)$ for $\theta_0 = 0$, ($n = 10$ and $n = 50$ marked with filled circles and diamonds respectively). Middle and right: $\gamma(\theta_0)$ for $k_y \rho_r = 0.05$ and 0.5 . Estimated Hahn–Burrell shearing rate $|\omega_{HB}|$ for each surface shown with thin lines.

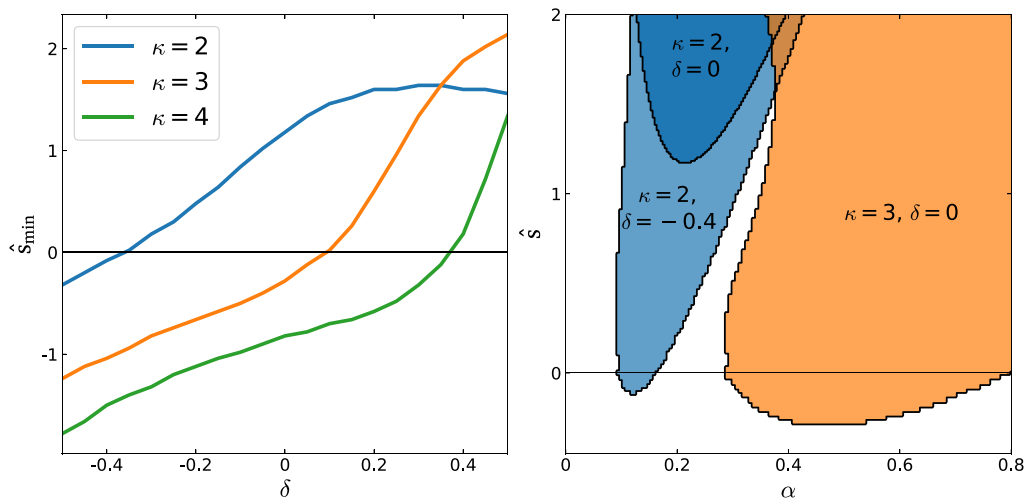


Figure 5. Left: dependence of second stability access window ($\hat{\delta}_{min}$) on elongation (κ) and triangularity (δ) for the $\psi_N = 0.5$ surface of ‘-ve tri’ equilibrium. Right: IBM unstable regions for $(\kappa, \delta) = (2, -0.4)$ (light blue), $(2, 0)$ (dark blue), $(3, 0)$ (orange).

4.1. Second stability access in the negative triangularity regime

Section 4 supports a simple picture: KBM growth rates tracking IBM stability, and likely unacceptably high for steady-state operation. This prompts the question: is the closing of second stability a general feature of negative triangularity STs, or could a configuration exist with second stability access?

To test this we parametrise the $\psi_N = 0.5$ surface using the model developed by Miller *et al* [31], which provides an analytic description of the flux surface in terms of nine dimensionless parameters (‘Miller parameters’) (a description of our parametrisation process is given in appendix C). We then test the effect of varying the triangularity (δ) and elongation (κ) in isolation, and find (in agreement with [13]) that this strongly affects stability. The role of reducing δ is to reduce $\hat{\delta}_{min}$ and reduce α_{crit} i.e. to close the second stability window and shrink the first stability region. For negative δ , the effect of increasing κ is to increase α_{crit} but reduce $\hat{\delta}_{min}$. This is illustrated in figure 5.

These results indicate that, where ballooning modes are concerned, $\delta < 0$ is not an attractive option, unless

β is sufficiently low that the equilibrium remain in the first stable region. For $\psi_N = 0.5$ for example, $\alpha_{crit} = 0.16$, compared with the equilibrium value of $\alpha = 0.42$. Fixing the plasma size, a low- β device would require a large magnetic field. While high temperature superconductors may provide a possible pathway, they present engineering challenges.

It should be noted that the other Miller parameters, such as q , also affect $\hat{\delta}_{min}$. A general study of the parametric dependencies of the IBM is beyond the scope of this work, but we note that relatively large changes to the Miller parameters of this surface are required to open second stability at fixed (δ, κ) . As an example, achieving $\hat{\delta}_{min} > 0$ for our negative triangularity scenario requires increasing q from 3.0 to 5.4 with all other parameters kept fixed.

We also explored adjusting the magnitude of the local Shafranov shift parameter, $|\partial R_0 / \partial \psi_N|$. This is generally higher in the positive triangularity equilibria than for negative triangularity (e.g. ‘high q ’ has 10% greater shift than ‘-ve tri’ at $\psi_N = 0.5$), probably due to the reduced core pressure in the latter, and one may wonder whether this modifies

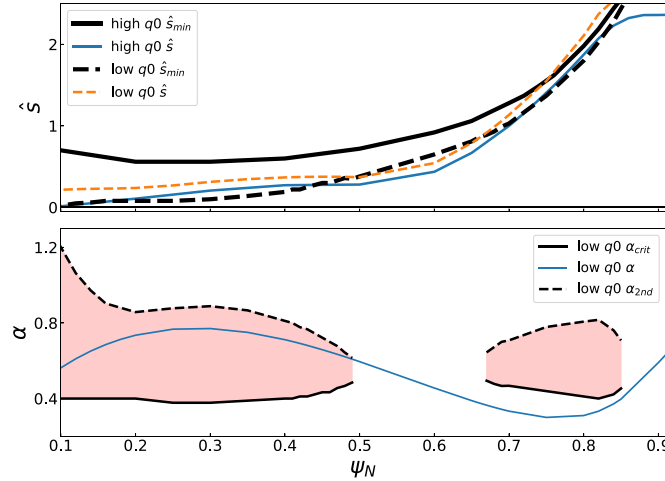


Figure 6. Upper: \hat{s} and \hat{s}_{min} for the positive triangularity equilibria. Lower: α , α_{crit} and α_{2nd} for the ‘low $q0$ ’ equilibrium. NB for ‘high $q0$ ’, $\hat{s} < \hat{s}_{min}$ for all values of ψ_N , so α_{crit} and α_{2nd} is undefined.

stability. We found that \hat{s}_{min} decreased (i.e. became more negative) as the magnitude of shift increased from its original Miller-fitted value. Whilst this is not exactly the same as recalculating the global equilibrium with an increased core β_N , this result suggests that attempting to operate at higher β is unlikely to alleviate the problem of second stability access.

5. Stability properties of positive triangularity equilibria

We now consider the positive triangularity equilibria. Consistent with remarks made in section 4.1, we find these have better IBM stability, with $\hat{s}_{min} > 0$ everywhere as shown in figure 6. Despite this, ‘low $q0$ ’ is unstable near the magnetic axis ($\psi_N < \sim 0.5$), illustrating the importance of current distribution (via its effect on q) on ballooning stability. A ‘high $q0$ ’ is achieved with a hollow current profile, and this is IBM-stable across the plasma.

The gyrokinetic $\gamma(\psi_N)$ (shown in figure 7) show similar behaviour between ‘high $q0$ ’ and ‘low $q0$ ’ for $\psi_N > \sim 0.5$ (consistent with the similarity of q, κ, δ). In this region, instabilities with shorter wavelengths ($k_y \rho_r \sim 0.5$) are dominant for $\theta_0 = 0$, peaking near the pedestal top. However, as shown in figure 8, $\gamma(\theta_0)$ is very narrow, and hence highly susceptible to $\mathbf{E} \times \mathbf{B}$ shear stabilisation.

However, $\gamma(\psi_N)$ differs in the core ($\psi_N < \sim 0.5$), coinciding with differences in IBM stability. ‘low $q0$ ’ exhibits a long-wavelength ‘ideal’ KBM ($\gamma(k_y \rho_r)$ shown in figure 8), consistent with the plasma being on or over the ideal ballooning boundary. ‘high $q0$ ’ has small but finite γ at long wavelength. Identification of these dominant instabilities is discussed in the following section.

For both equilibria, $\gamma(\psi_N)$ is lower than for ‘-ve tri’, unstable over a smaller range of $k_y \rho_r$ (figure 8) and of similar magnitude to $|\omega_{HB}|$ over much of the plasma. This represents a dramatic improvement in microstability, as a direct result of making the triangularity positive.

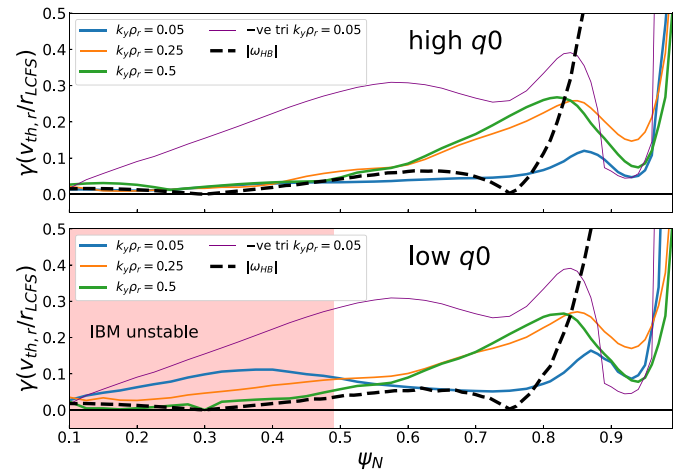


Figure 7. $\gamma(\psi_N, k_y \rho_r)$ for ‘high $q0$ ’ (upper) and ‘low $q0$ ’ (lower) with $\theta_0 = 0$. ‘-ve tri’ ($k_y \rho_r = 0.05$) shown for comparison (thin purple line). All growth rates normalised to $v_{th,r}/r_{LCFS}$ for their own flux surface and equilibria. Dashed black line indicates approximate magnitude of Hahn–Burrell shearing rate $|\omega_{HB}|$. Shaded region indicates ideal MHD ballooning unstable surfaces.

6. Instability identification

6.1. Negative triangularity

Here we seek to identify the core and pedestal instabilities in the ‘-ve tri’ equilibrium, by considering ($k_y \rho_r = 0.05$, $\theta_0 = 0$) for the $\psi_N = 0.5$ (core) and $\psi_N = 0.9$ (pedestal) flux surfaces.

We first verify that the dominant instability tracks the IBM stability boundary in \hat{s} - α space (as shown in figure 9). For both surfaces, the complex frequency Ω tracks the IBM boundary fairly well; γ is high across the unstable region and the frequency is smooth and in the ion diamagnetic direction¹.

¹ To self-consistently change α , one must scale the simulation value of β and/or the normalised kinetic gradients ($n'_{i,e}/n_{i,e}$, $T'_{i,e}/T_{i,e}$). Both of these choices are shown in figure 9.

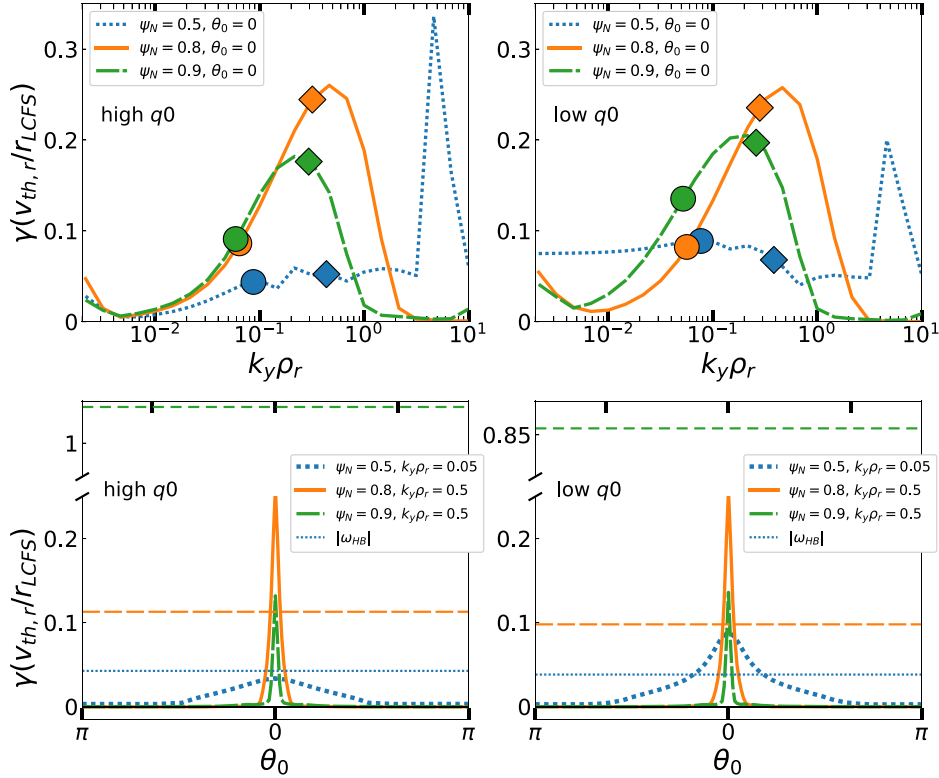


Figure 8. Upper row: $\gamma(k_y \rho_r)$ for ‘high q_0 ’ (left) and ‘low q_0 ’ (right) for several ψ_N , $\theta_0 = 0$. $n = 10$ and $n = 50$ marked with filled circles and diamonds respectively. Lower row: $\gamma(\theta_0)$ for selected ψ_N , $k_y \rho_r$ for ‘high q_0 ’ (left) and ‘low q_0 ’ (right). Estimated Hahn–Burrell shearing rate $|\omega_{HB}|$ shown with thinner horizontal lines.

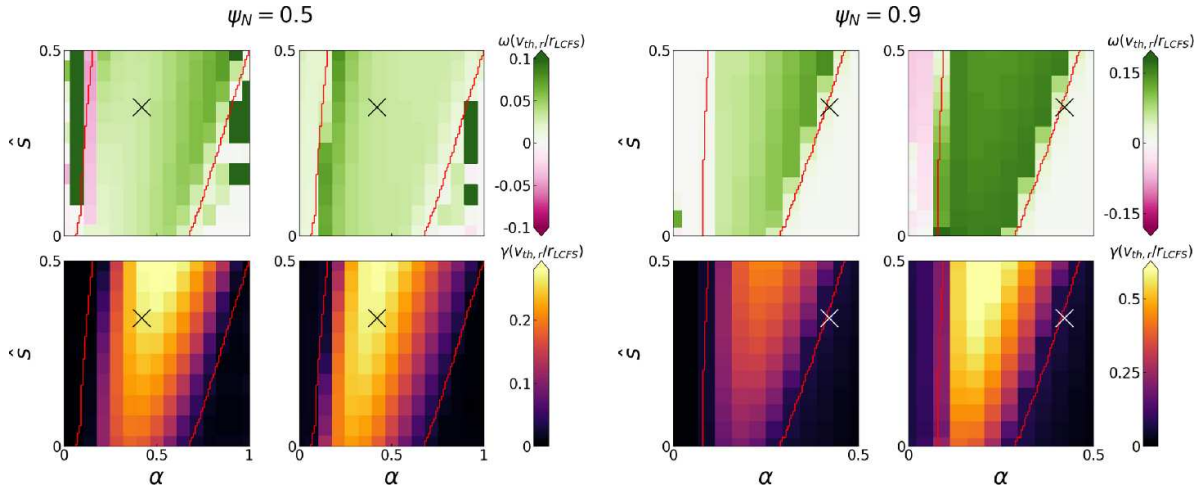


Figure 9. Gyrokinetic \hat{s} - α plot for the $\psi_N = 0.5$ (left 4 plots) surface of ‘-ve tri’ equilibrium ($k_y \rho_r = 0.05, \theta_0 = 0$) and $\psi_N = 0.9$ (right 4 plots). Top row shows mode frequency ω and lower shows growth rate γ . Left column: fixed β . Right column: fixed gradients. Cross marks equilibrium \hat{s} , α .

We also tested whether the mode was sensitive to α , but not specific contributions ($\partial T/\partial \psi_N$, $\partial n/\partial \psi_N$, β). This was done by scanning the quantity $f \equiv \beta \cdot (1/T) \cdot (\partial T/\partial \psi_N)$, in three cases: (1) scaling $(1/T) \cdot (\partial T/\partial \psi_N)$ at fixed β , adjusting $(1/n) \cdot (\partial n/\partial \psi_N)$ to keep α constant (2) scaling $(1/T) \cdot (\partial T/\partial \psi_N)$ at fixed β but keeping $\eta \equiv (n \cdot \partial T/\partial \psi_N)/(T \cdot \partial n/\partial \psi_N)$ fixed (such that f changes α , with $f = 0$ corresponding to $\alpha = 0$) (3) keeping the gradients constant but

scaling β . In all cases, we kept the magnetic geometry constant i.e. not changed to be consistent with α .

The result of this scan (shown in figure 10) shows Ω and the parallel electric field $\max(E_{\parallel}(\theta)) \equiv \max(-\partial \phi/\partial \theta - \partial A_{\parallel}/\partial t)$ (normalised to the electrostatic potential ϕ) are constant with f when α is fixed (case 1). Cases (2) and (3) demonstrate that the kinetic gradients and β are approximately interchangeable in driving the mode (provided $\beta > 0$). Moreover, the normalised

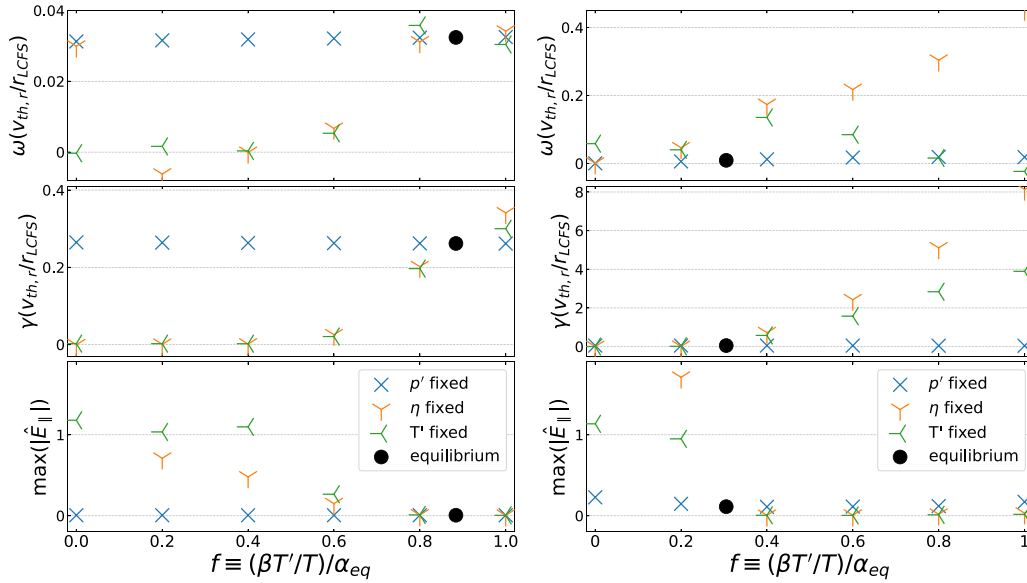


Figure 10. ‘-ve tri’ equilibrium with $k_y \rho_r = 0.05, \theta_0 = 0$. Left: $\psi_N = 0.5$. Right: $\psi_N = 0.9$. Scanning $f \equiv \beta \cdot (1/T) \cdot (\partial T / \partial \psi_N)$ for (1) fixed α and β (blue crosses), (2) fixed η and β (orange (Y)), (3) fixed gradients (green (Y)). Equilibrium value of f shown as black filled circle.

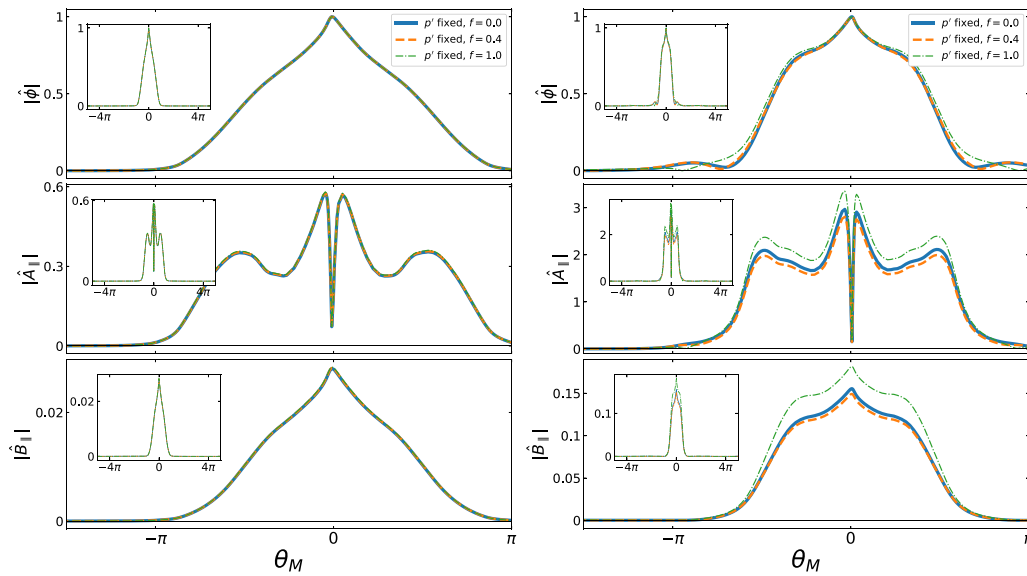


Figure 11. Mode structures for ‘-ve tri’ equilibrium for $\psi_N = 0.5$ (left) and $\psi_N = 0.9$ (right), with $k_y \rho_r = 0.05, \theta_0 = 0$ as f scanned. θ_M is a poloidal coordinate, defined as $\theta_M = \sin^{-1}(Z / (\kappa \cdot r_{\text{minor}}))$, where κ, r_{minor} are the geometric elongation and minor radius of the flux surface respectively.

mode structures ($|\hat{\phi}(\theta)|$, $|\hat{A}_{\parallel}(\theta)|$, $|\hat{B}_{\parallel}(\theta)|$) (figure 11) are virtually identical when f is scanned at fixed α for $\psi_N = 0.5$ and very similar for $\psi_N = 0.9$. This confirms the mode is indeed driven by α .

We conclude that the instability observed across the core is an ‘ideal MHD’-like KBM, with the following features: (a) γ tracks the ideal MHD boundary well (b) the frequency is in the ion diamagnetic direction (c) the mode has a low parallel electric field $E_{\parallel}(\theta)$, indicative of MHD-like modes [18] (d) the mode amplitude is greatest in the bad curvature region and (e) has twisting parity (f) the mode preferentially occurs at long wavelength (g) the mode structure and complex

frequency are sensitive to α but not to kinetic gradients or β individually. The pedestal, though IBM-stable, has all of the above properties, although γ is more sensitive to $(k_y \rho_r)$ at long wavelength (figure 4). We speculate this is a ‘non-ideal’ KBM, destabilised by some kinetic effect(s), allowing it to slightly exceed the ideal boundary.

6.2. Positive triangularity

We repeated this analysis for ($\psi_N = 0.5, k_y \rho_r = 0.05, \theta_0 = 0$) for the ‘high q_0 ’ and ‘low q_0 ’ equilibria. Departures from the ideal MHD stability boundary are seen in \hat{s} - α space

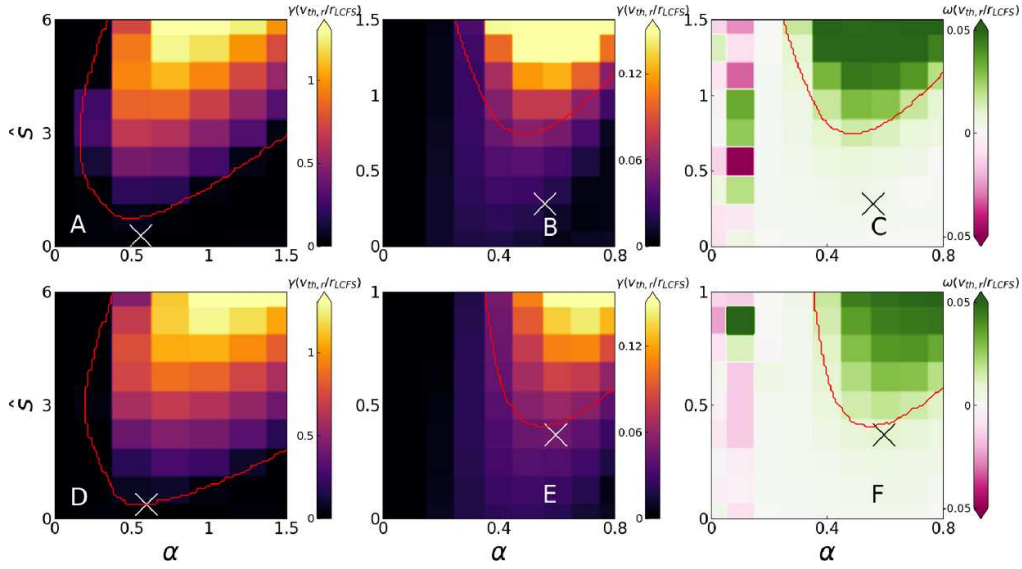


Figure 12. Gyrokinetic \hat{s} - α plots for the $\psi_N = 0.5$ surface for $k_y \rho_r = 0.05$, $\theta_0 = 0$ at fixed β . Top row: ‘high q_0 ’; $\gamma(\hat{s}, \alpha)$ over a large range (A), a small range (B) and $\omega(\hat{s}, \alpha)$ over a small range (C). Bottom row: ‘low q_0 ’; $\gamma(\hat{s}, \alpha)$ over a large range (D), a small range (E) and $\omega(\hat{s}, \alpha)$ over a small range (F). Crosses indicate equilibrium \hat{s} , α .

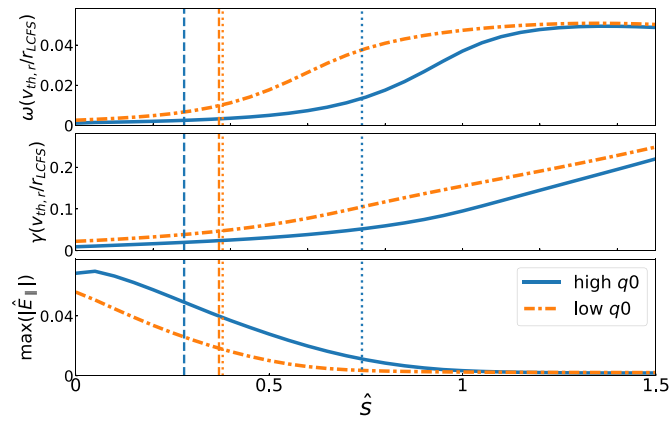


Figure 13. Upper: ω , γ , $\max(|\hat{E}_{\parallel}|)$ for the $\psi_N = 0.5$ flux surface for ‘high q_0 ’ and ‘low q_0 ’ ($k_y \rho_r = 0.05$, $\theta_0 = 0$) as \hat{s} is scanned. Equilibrium \hat{s} shown by vertical dashed lines and IBM marginal stability by vertical dotted lines.

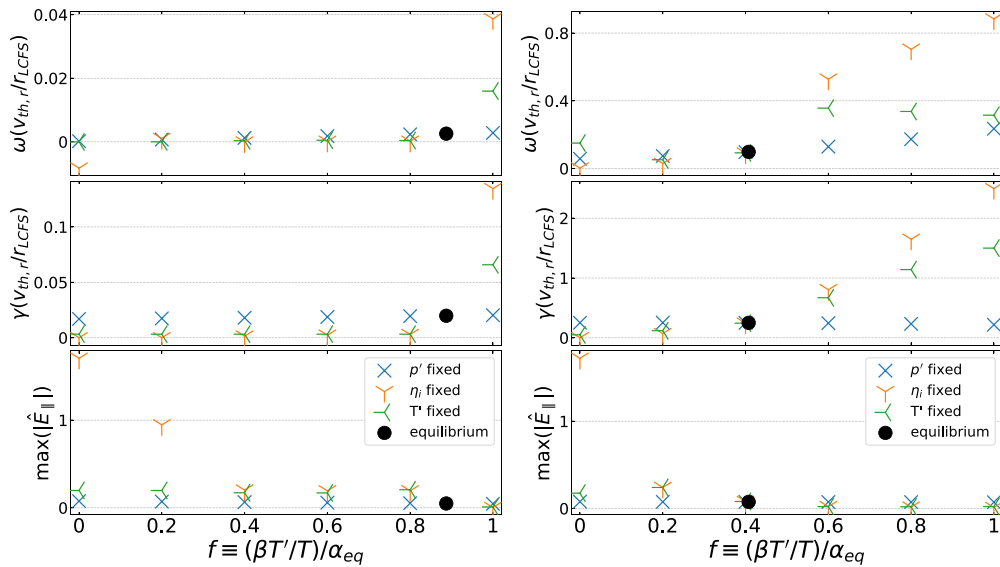


Figure 14. ‘high q_0 ’ equilibrium; ω , γ , $|\hat{E}_{\parallel}|$ as $f \equiv \beta \cdot (1/T) \cdot (\partial T / \partial \psi_N)$ is scanned. Left: $\psi_N = 0.5$, $k_y \rho_r = 0.05$, $\theta_0 = 0$. Right: $\psi_N = 0.8$, $k_y \rho_r = 0.5$, $\theta_0 = 0$.

(figure 12), with the KBM smoothly extending across the IBM boundary into the second stability window. To confirm this smooth transition, we performed a fine scan in \hat{s} , keeping α at its equilibrium value (shown in figure 13).

Like the KBMs discussed in section 6.1, the mode has a frequency in the ion diamagnetic direction and twisting parity. E_{\parallel} is low, but rises smoothly as \hat{s} leaves the IBM unstable region. Scanning $f \equiv \beta \cdot (1/T) \cdot (\partial T / \partial \psi_N)$ for ‘high q_0 ’ (figure 14), we again find the mode is α -driven. These features were also found for other flux surfaces sampled across the core, and for $k_y \rho_r = 0.5$ (f scan for $(\psi_N = 0.8, k_y \rho_r = 0.5)$ shown in figure 14). These observations support the conclusion that, although ideal ballooning stable, the dominant long-wavelength instability in these equilibria is a ‘non-ideal’ KBM.

7. Conclusions

In this work, we have assessed the ballooning stability of three hypothetical ST equilibria, constructed with a commercial power-producing reactor in mind. In all three cases, the normalised pressure gradient α is sufficiently high to exceed the first stable region for ballooning modes; the equilibrium is either in the unstable region, or in the second stability window. In the negative triangularity case, the second stability window does not exist at positive magnetic shear, meaning the plasma is ideal ballooning unstable across the core; this coincides with strongly growing KBMs and indicating that this is unlikely to be a feasible equilibrium in the context of transport. We have considered the dependency of second stability access on shaping parameters, and found that second stability may be obtained either by making triangularity more positive, or reducing the elongation. These point to KBMs prohibiting negative triangularity as an option in commercial STs, unless they can be operated at very high field (which then introduces engineering challenges).

The equilibria with positive triangularity show better stability properties. In these, second stability access exists across the plasma and, provided the on-axis safety factor is not too low, the equilibrium occupies the second stability window across its full radius. Microinstability growth rates are correspondingly low. However, there remains a weakly growing instability with KBM-like properties, namely: pressure-driven, twisting parity, smoothly connecting to the ‘ideal MHD’ KBM, low parallel electric field and, in some cases, the modes are pervasive at long wavelength. We speculate that the KBM is destabilised by kinetic effects. Being weakly growing, these could feasibly be stabilised by flow shear or may impose a soft β limit on STs. Identifying these effects would be an interesting area of future work, and may be necessary if one wished to build a predictive model of ST H-mode pedestals in a similar manner to EPED [32].

Data availability statement

The data that support the findings of this study are available upon reasonable request from the authors.

Acknowledgments

The authors are grateful for productive discussions with M Anastopoulos-Tzanis, B Patel, C M Roach, B F McMillan and S Biggs-Fox. This work was supported by the Engineering and Physical Sciences Research Council (EP/L01663X/1) and (EP/R034737/1). This project was undertaken on the Viking Cluster, which is a high performance compute facility provided by the University of York. We are grateful for computational support from the University of York High Performance Computing service, Viking and the Research Computing team. This research used the GS2 version latest commit 142c78781c1bc4c06d234b32fee70eaf100d68e4 (8.1).

Appendix A. Estimation of $E \times B$ flow shearing rate

We use an approach similar to that used by Applegate *et al* [27]. We take the shearing rate as

$$\omega_{\text{HB}} = \frac{(\partial \psi / \partial r_{\text{minor}})^2}{B} \frac{\partial^2 \Phi}{\partial \psi^2}, \quad (\text{A.1})$$

where B is the magnetic field strength and Φ is the equilibrium electrostatic potential. We estimate Φ by taking the equilibrium force balance

$$\frac{\nabla p}{n_i e} = \mathbf{V} \times \mathbf{B} + \mathbf{E}, \quad (\text{A.2})$$

(where p is the ion pressure, $\eta_i = (T_i' n_i) / (T_i n_i')$, denoting a derivative with respect to ψ , \mathbf{V} the ion flow velocity and \mathbf{E} the equilibrium electric field), and setting $\mathbf{V} = 0$. A little manipulation yields

$$\omega_{\text{HB}} = \frac{(\partial \psi / \partial r_{\text{minor}})^2}{B \cdot n_i e} \left(\frac{\partial^2 p}{\partial \psi^2} + \frac{1}{p \cdot (1 + \eta_i)} \left(\frac{\partial p}{\partial \psi} \right)^2 \right). \quad (\text{A.3})$$

We take B as the field strength on the surface at the location of the magnetic axis.

Appendix B. Simulation parameters and tests

Since the data used for these simulations is publicly available, we only describe noteworthy parameters here. Their values were chosen to minimise computational cost without compromising accuracy of the simulations; we justify our choice by comparing a selection of $(\psi_N, k_y \rho_r, \theta_0)$ for the three equilibria to higher-fidelity simulations. In particular, the difference in growth rate $\Delta \gamma = \gamma_0 - \gamma_{\text{hf}}$ (where γ_0 is the growth rate found with our parameters used and γ_{hf} the growth rate for a higher-fidelity simulation) is used as a figure of merit. In some cases $\gamma_{0,\text{hf}}$ is low, resulting in large fractional errors, so here we quote the absolute error (in normalised units of $v_{\text{th},r} / r_{\text{LCFS}}$).

The parameters governing the parallel coordinate θ are `nperiod` = 3, `ntheta` = 192 (although it was sometimes necessary to adjust `ntheta` owing to difficulties encountered

in **GS2**'s **gridgen** module). The former specifies the extent of the simulation domain in ballooning space ($\theta = -5\pi$ to $\theta = 5\pi$ in our case). This is insufficient to resolve extended micro-tearing structures which have been seen in high- β equilibria [22], but reasonable for KBMs. Preliminary research did not reveal any extended structures at long wavelength. Comparing **nperiod** = 3 to **nperiod** = 5 we found $\max(|\Delta\gamma|) = 4 \times 10^{-3}$ with rms value $\Delta\gamma_{\text{rms}} \equiv \sqrt{\sum_N (\Delta\gamma)_N^2 / N} = 4 \times 10^{-4}$. Comparing **ntheta** = 192 to **ntheta** = 394, we found $\Delta\gamma_{\text{rms}} = 5 \times 10^{-3}$ for $\psi_N \leq 0.9$ and $\Delta\gamma_{\text{rms}} = 0.02$ for $\psi_N > 0.9$, reflecting a difficulty in the calculation of geometric quantities in **GS2** for strongly-shaped numerically-prescribed surfaces.

The equilibrium data contains density profiles $n(\psi_N)$ for electrons, the main ion species (with a mass of 2.5 times the proton mass and $Z = 1$), helium ash and two impurity species: tungsten (with typical density $n_W/n_e \sim 10^{-5}$) and xenon ($n_X/n_e \sim 10^{-4}$) (both assumed fully ionised). Lacking simulated temperature profiles, it was assumed that $T(\psi_N)$ is identical for all species (the effect of fast ions may be an interesting area of future research.) Comparing simulations with the five kinetic species to the 'reduced' simulation with two

kinetic species (in which $n_i = n_e$ to ensure quasi-neutrality), we found $\Delta\gamma_{\text{rms}} = 0.02$.

Collisions were ignored in the results presented here. Comparing collisionless to collisional simulations, we found $\Delta\gamma_{\text{rms}} = 0.01$ for $\psi_N \leq 0.9$ and $\Delta\gamma_{\text{rms}} = 0.09$ for $\psi_N > 0.9$ (consistent with the lower temperatures, and hence increased collisionality, near the edge).

Appendix C. Miller parametrisation

The Miller parametrisation [31] describes each surface by nine dimensionless parameters: aspect ratio A , elongation κ , triangularity δ , the radial derivatives of major radius, elongation and triangularity s_κ , s_δ , $\partial R_0/\partial\psi_N$, the safety factor q , normalised magnetic shear $\hat{s} \equiv \partial q/\partial\psi_N$, and normalised pressure gradient $\alpha \equiv -\partial\beta/\partial\psi_N$. These specify the shape of the flux surface and its poloidal magnetic field:

$$R = R_0 + r \cos[\theta_M + x \sin\theta_M], \quad (\text{C.1})$$

$$Z = \kappa r \sin\theta_M, \quad (\text{C.2})$$

$$B_p = \frac{(\partial\psi/\partial r)\kappa^{-1}R^{-1}[\sin^2(\theta_M + x \sin\theta_M)(1 + x \cos\theta_M)^2 + \kappa^2 \cos^2\theta_M]^{1/2}}{\cos(x \sin\theta_M) + (\partial R_0/\partial r) \cos\theta_M + [s_\kappa - s_\delta \cos\theta_M + (1 + s_\kappa)x \cos\theta_M] \sin\theta_M \sin(\theta_M + x \sin\theta_M)}, \quad (\text{C.3})$$

where R and Z are cylindrical coordinates (with the magnetic axis located at $Z = 0$), B_p the poloidal magnetic field and θ_M a poloidal coordinate ranging from 0 to 2π .

We fit Miller parameters to the numerical SCENE flux surface data as follows. Firstly, the numerical values of R , Z and B_p for the flux surface of interest are extracted from the SCENE data. R and Z are used to construct θ_{geo} , a poloidal coordinate defined by $\theta_{\text{geo}} = \arctan((Z - Z_{\text{maxis}})/(R - R_{\text{maxis}}))$, where $(R_{\text{maxis}}, Z_{\text{maxis}})$ is the location of the magnetic axis, and is taken from the SCENE equilibrium. Splines of $R(\theta_{\text{geo}})$ and $Z(\theta_{\text{geo}})$ are used to upsample R and Z , and from this calculate the values for A , r , κ , δ and construct Miller's poloidal coordinate by defining

$$\theta_M \equiv \arcsin((Z - Z_{\text{maxis}})/(\kappa r)). \quad (\text{C.4})$$

$B_p(\theta_M)$ is then constructed and fitted to equation (C.3), with fitting parameters s_κ , s_δ , $\partial_r R_0$, $\partial\psi/\partial r$ (the latter determining q).

The above process yields an estimate of the Miller parameters describing a particular surface. However, it treats the parameters (A, r, κ, δ) on a different footing to $(s_\kappa, s_\delta, \partial_r R_0, q)$; calculating the former from R and Z does not guarantee an optimal fit of B_p , or indeed of (R, Z) (since most of the R, Z

points are ignored.) Therefore, we apply an additional step of simultaneously fitting $(R_M(\theta_M), Z_M(\theta_M), B_{pM}(\theta_M))$ to $(R(\theta_M), Z(\theta_M), B_p(\theta_M))$ allowing all eight parameters to vary freely, using the previously calculated values as initial guesses. This method ensures that B_p is treated on the same footing as R and Z , at the expense of allowing (A, r, κ, δ) to deviate from their geometric values.

Finally, the values of \hat{s} and α are selected. Since (R, Z, B_p) do not depend on (\hat{s}, α) , these can be scanned independently in **GS2**.

A caveat of the scheme presented above is that for reasons of convenience, we use the numerical equilibrium value of q rather than the value derived from $\partial_r R_0$.

Plots of the Miller parametrisation for several flux surfaces for each equilibrium are shown in figure C1. $R, Z, B_p(\theta_M)$ and (R, Z) show good agreement between the SCENE data and Miller fit in the core, with slightly worse agreement towards the edge; in particular, the fitted B_p for the '-ve tri' has a tendency to artificially peak on the inboard side. Another systematic feature of the fitting is that the elongation tends to be underestimated in the positive triangularity cases and overestimated in the negative triangularity case, with the effect becoming more exaggerated at higher ψ_N .

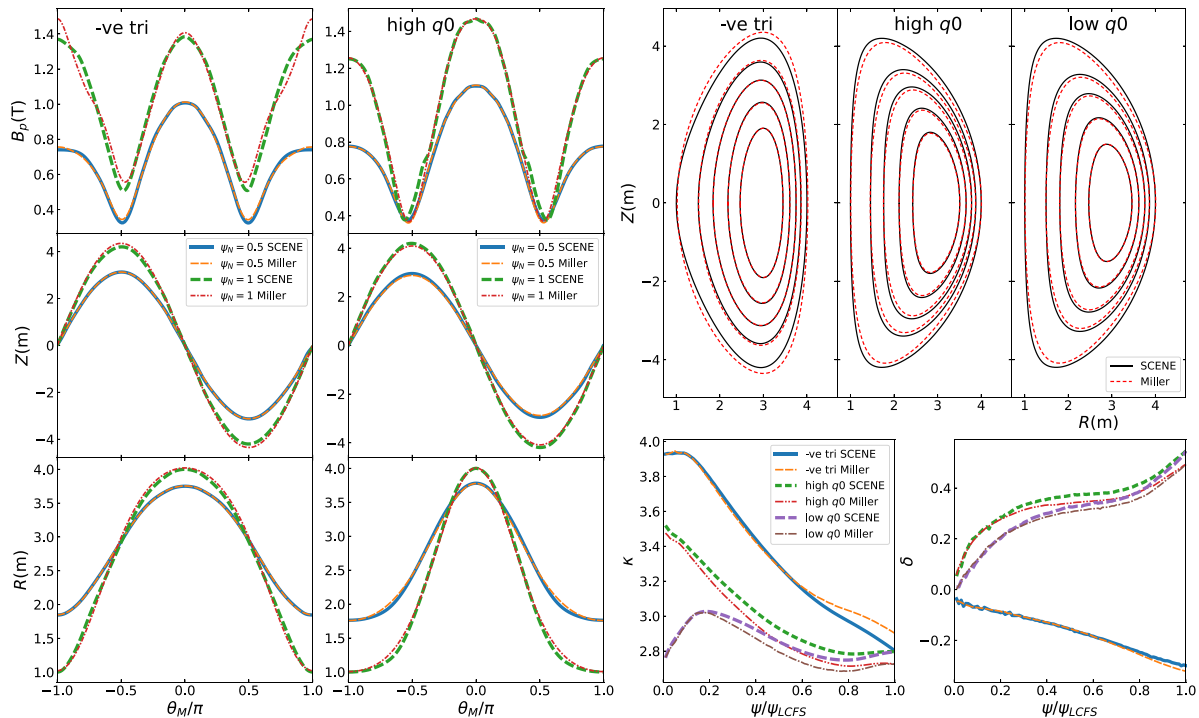


Figure C1. Comparison of numerical equilibria data generated by SCENE to Miller parametrisation. Left: R , Z , B_p as a function of poloidal coordinate θ_M . Right, upper: flux surface shape for $\psi_N = (0.15, 0.3, 0.5, 0.7, 1)$. Right, lower: elongation (κ) and triangularity (δ) vs ψ_N ; calculated directly from SCENE data and Miller parametrised.

ORCID iDs

R Davies <https://orcid.org/0000-0001-5570-5882>
 D Dickinson <https://orcid.org/0000-0002-0868-211X>
 H Wilson <https://orcid.org/0000-0003-3333-7470>

References

- [1] Peng Y-K M and Strickler D 1986 *Nucl. Fusion* **26** 769–77
- [2] Akers R *et al* 2000 *Nucl. Fusion* **40** 1223–44
- [3] Gryaznevich M P and Sharapov S E 2004 *Plasma Phys. Control. Fusion* **46** S15–S29
- [4] Costley A E and McNamara S A M 2021 *Plasma Phys. Control. Fusion* **63** 035005
- [5] Kaye S *et al* 2019 *Nucl. Fusion* **59** 112007
- [6] Gryaznevich M (Tokamak Energy team) 2019 *AIP Conf. Proc.* **2179** 020008
- [7] Harrison J *et al* 2019 *Nucl. Fusion* **59** 112011
- [8] Doyle S *et al* 2021 *Fusion Eng. Des.* **171** 112706
- [9] Banks M 2021 *Phys. World* **34** 10ii
- [10] Fontana M, Porte L, Coda S and Sauter O (The TCV Team) 2018 *Nucl. Fusion* **58** 024002
- [11] Austin M E *et al* 2019 *Phys. Rev. Lett.* **122** 115001
- [12] Saarelma S, Austin M E, Knolker M, Marinoni A, Paz-Soldan C, Schmitz L and Snyder P B 2021 *Plasma Phys. Control. Fusion* **63** 105006
- [13] Medvedev S *et al* 2015 *Nucl. Fusion* **55** 063013
- [14] Wilson H *et al* 2004 *Nucl. Fusion* **44** 917–29
- [15] Frieman E A, Rewoldt G, Tang W M and Glasser A H 1980 *Phys. Fluids* **23** 1750–69
- [16] Tang W, Connor J and Hastie R 1980 *Nucl. Fusion* **20** 1439–53
- [17] Aleynikova K and Zocco A 2017 *Phys. Plasmas* **24** 092106
- [18] Tang W, Rewoldt G, Cheng C and Chance M 1985 *Nucl. Fusion* **25** 151–64
- [19] Wilson H, Dickinson D, Patel B and Anastopoulos Tzani M S 2021 TDoTP high-beta ST plasma equilibria *Zenodo* (available at: <https://zenodo.org/record/4643844>)
- [20] Wilson H 1994 SCENE—simulation of self-consistent equilibria with neoclassical effects *Technical Report UKAEA-FUS-271* (Culham: UKAEA Govt. Division, Fusion)
- [21] Barnes M *et al* 2021 Gs2 v8.1.0 Supported by CCP Plasma (available at: <https://gow.jpgrc.ukri.org/NGBOViewGrant.aspx?GrantRef=EP/M022463/1>) and HEC Plasma (available at: <https://gow.jpgrc.ukri.org/NGBOViewGrant.aspx?GrantRef=EP/R029148/1>) <https://doi.org/10.5281/zenodo.5772100>
- [22] Patel B, Dickinson D, Roach C and Wilson H 2022 *Nucl. Fusion* **62** 016009
- [23] Dimits A, Cohen B, Mattor N, Nevins W, Shumaker D, Parker S and Kim C 2000 *Nucl. Fusion* **40** 661–6
- [24] Abel I G, Plunk G G, Wang E, Barnes M, Cowley S C, Dorland W and Schekochihin A A 2013 *Rep. Prog. Phys.* **76** 116201
- [25] Kotschenreuther M, Rewoldt G and Tang W 1995 *Comput. Phys. Commun.* **88** 128–40
- [26] Hahm T S and Burrell K H 1995 *Phys. Plasmas* **2** 1648–51
- [27] Applegate D J *et al* 2004 *Phys. Plasmas* **11** 5085–94
- [28] Ida K and Rice J 2014 *Nucl. Fusion* **54** 045001
- [29] Rice J 2016 *Plasma Phys. Control. Fusion* **58** 083001
- [30] Pueschel M J, Terry P W, Jenko F, Hatch D R, Nevins W M, Görler T and Told D 2013 *Phys. Rev. Lett.* **110** 155005
- [31] Miller R L, Chu M S, Greene J M, Lin-Liu Y R and Waltz R E 1998 *Phys. Plasmas* **5** 973–8
- [32] Snyder P, Groebner R, Hughes J, Osborne T, Beurskens M, Leonard A, Wilson H and Xu X 2011 *Nucl. Fusion* **51** 103016